ACS Catalysis

Research Article

pubs.acs.org/acscatalysis

Design of Highly Active Perovskite Oxides for Oxygen Evolution Reaction by Combining Experimental and ab Initio Studies

Min Ho Seo,[†] Hey Woong Park,[†] Dong Un Lee, Moon Gyu Park, and Zhongwei Chen*

Department of Chemical Engineering, Waterloo Institute for Nanotechnology, Waterloo Institute of Sustainable Energy, University of Waterloo, 200 University Avenue W, Waterloo, Ontario N2L 3G1, Canada

Supporting Information

ABSTRACT: Perovskite oxides (ABO_3) have recently attracted attention since tailoring their chemical compositions has resulted in remarkable activity toward oxygen evolution reaction (OER) which governs rechargeability of recently spotlighted metal−air batteries and regenerative fuel cells. For further development of highly OER active perovskite oxides, however, the exact mechanism the OER must be well understood. Herein, we introduce investigation of the OER mechanism of perovskite oxides by ab initio analysis based on well-defined model systems of $LaMnO_3$ (LMO), $LaCoO_3$ (LCO), and $La_{0.5}Sr_{0.5}CoO_3$ (LSCO). In addition, we have systematically conducted electrochemical experiments from which we have observed an increasing trend in the OER activity in the order of LSCO > LCO > LMO based on the cyclic voltammetry (CV) results obtained in the alkaline medium. To validate the experimental results, free-energy diagrams have been constructed for oxygen intermediates on the surface of the defined models to find the limiting step by changing the B site atom (e.g., Mn and Co) and the partial displacement of Sr atoms in La site. The oxygen adsorption energy of perovskite oxides is found to increase with decreasing number of outer electrons as well as upshifting of the position of the d_{z^2} orbital toward the Fermi level of B site element. This work demonstrates that highly active OER perovskite oxides can be obtained by modifying the chemical composition to finely tune the oxygen adsorption energy on the catalyst's surface, confirmed by synergetic approaches of using both experimental and ab initio computational studies.

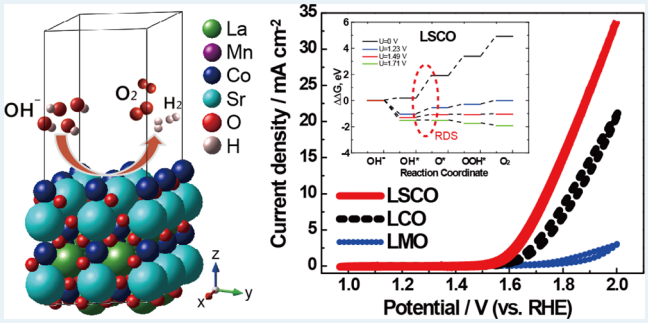

KEYWORDS: *metal−air battery, oxygen evolution reaction, perovskite oxide, electrocatalyst, density functional theory, ab initio calculation*

Development of highly active electrocatalysts that are cost competitive takes the center stage in research fields for next-generation electrochemical energy conversion and storage systems.[1−5] These systems have extremely important environmental implications on reducing global warming and facilitating sustainable energy generation.[1−3] Among many electrochemical processes, oxygen evolution reaction (OER) is a significantly important process since it directly governs rechargeability of recently spotlighted metal-air batteries and regenerative fuel cells.[1−3] However, the intrinsically sluggish kinetics of OER significantly limits performance of these advanced energy devices.[6,7] Perovskite oxide, which has the chemical formula ABO_3 consisting of rare earth and alkaline earth in the A site and 3d transition metal in the B site, has drawn tremendous attention due to its remarkable OER activity that is comparable to that of precious metal based catalysts such as iridium and ruthenium supported on carbon.[8,9] Despite their excellent electrocatalytic activity, its origin is still unclear, which must be clearly understood in order to further improve the catalysts. Due to the lack of clear mechanistic understanding, current catalyst research largely progresses in a trial-and-error manner, where a novel composition with a specific geometry is physicochemically and electrochemically analyzed to screen for adequate catalytic performance. This traditional experimental approach may not be efficient because of its difficulty to control the structure and surface properties of electrocatalysts as well as to verify electronic and geometric structure ion the atomic scale.[10] On the other hand, the theoretical approach by ab initio computational methods (DFT) is useful for describing the underlying mechanisms of experimentally observed complicated surface reactions. Representatively, the d-band center model proposed by Nørskov and associates has successfully proven to provide information on the electronic structures of metal based heterogeneous catalysts which is strongly correlated to adsorption energy between catalyst surface and the adsorbate.[11,12] Fundamental studies using DFT along with experimental confirmation have been commonly done to explain the activity of oxygen reactions for metal-based catalysts, even including electrochemical stability issues of catalyst with/without support in acidic condition.[13−15] For

Received: January 20, 2015
Revised: May 26, 2015
Published: June 1, 2015

DOI: 10.1021/acscatal.5b00114
ACS Catal. 2015, 5, 4337−4344

metal oxides based catalysts, however, the prediction of catalytic activity and stability is difficult without structural data obtained by characterization of experiments. This is because thermodynamically stable structure is very difficult to define only by DFT due to structural complexity associated with different elements of metal oxides.[16,17] Therefore, a synergetic approach using both experimental and ab initio computational studies with physicochemical analyses is required to efficiently and accurately develop a new catalyst with highly improved activity.

The purpose of this work is to guide the design of highly efficient perovskite oxide catalysts active toward OER by elucidating the reaction mechanism governing the material's electrocatalytic performance. To accomplish this, $LaCoO_3$ (LCO) is chosen as the baseline perovskite oxide composition. As extensions of LCO, half of the La atoms in the A site are partially substituted by Sr, and Co in the B site is replaced by Mn to create $La_{0.5}Sr_{0.5}CoO_3$ (LSCO) and $LaMnO_3$ (LMO), respectively. This set of perovskite oxides (LMO, LCO, and LSCO) allow for investigation of effectiveness of modifying the A and B sites on improving catalytic activity toward OER. All perovskite oxides in this study are prepared by a simple solution-based calcination method. Furthermore, we have found the most thermodynamically stable structures of LMO, LCO, and LSCO for accurate DFT calculations by generating every configuration of the structures in a given unit cell by a method reported in the literature previously.[13,18,19] Furthermore, the hybrid-functional approach using the strongly correlated electrons has been employed by the Hubbard U correction (DFT+U) for more realistic models in order to correct the electron self-interaction error in generalized gradient approximation (GGA).[17,20,21] To compare with calculated thermodynamics results, we have experimentally evaluated electrochemical OER activity of LMO, LCO, and LSCO using rotating ring disk electrode half-cell testing.

For transition metal oxides, finding an energetically minimized crystal structure is necessary since the structure can change depending on the elemental composition. To define the most thermodynamically stable LSCO structure in the bulk, we have generated 22 configurations of different Sr amounts, which partially displaces La atoms in the A site of the perovskite oxide. Among them, six structures having La to Sr composition ratio of 1:1 in ABO_3 structure have been chosen to find the one with the lowest ground state energy as shown in Figure S1. The unit crystal structures of the fully relaxed ground state of LMO, LCO, and LSCO are illustrated in Figure 1 each of which has the minimum DFT energy, indicating the most thermodynamically stable structure. The models of LMO, LCO, and LSCO are then designed based on the crystal structures observed experimentally by X-ray diffraction (XRD) patterns shown in Figure 2a. Experimentally, the perovskite oxides have been prepared by a simple calcination method as illustrated in Figure S2, and their elemental compositions have been confirmed by XPS analysis as shown in Figure S3. Confirmation of space group of experimentally synthesized material is necessary to accurately compare with DFT results since the space group of perovskite structures can change depending on the synthetic method and synthesis conditions.[22,23] The experimentally observed XRD patterns of the perovskite oxides indeed match those calculated based on the lattice information obtained from the inorganic crystal structure database (ICSD). The space groups of LCO and LMO perovskite oxides calculated based on the XRD patterns obtained from ICSD shown in Figure 2b and c are found to be $R\bar{3}ch$ (nos. 80370 and 180176), whereas Figure S4a and b have the $pm\bar{3}m$ group (nos. 29119 and 28921). LCO having the $R\bar{3}ch$ space group shows intrinsic splitting of the dominant peak which corresponds to the (110) reflection, whereas only a single peak is observed with LCO having the $pm\bar{3}m$ space group. LMO and LCO having the $pm\bar{3}m$ space group in Figure S4a and b demonstrate relatively higher intensity peaks around 58°, corresponding to (214) reflection, compared with those having the $R\bar{3}ch$ space group shown in Figure 2. Consequently, these results clearly demonstrate that our prepared perovskite oxides belong to the $R\bar{3}ch$ space group with trigonal/rhombohedral symmetric structure. Theoretically calculated lattice parameters for *x*, *y*, and *z*-axes in the ground state of each perovskite oxides respond to 5.636, 5.650, and 13.42 Å for LMO; 5.545, 5.544, and 13.24 Å for LCO; and 5.541, 5.538, and 13.30 Å for LSCO, respectively. The lattice parameters of LSCO (no. 93380) exhibit reduction in *x* and *y*-axes, while elongation in *c*-axis due to the addition of Sr atoms in the A site. The XRD results of LMO, LCO, and LSCO calculated based on ICSD, therefore, are in good agreement with those of the synthesized perovskite oxides as well as previous experimental reports.

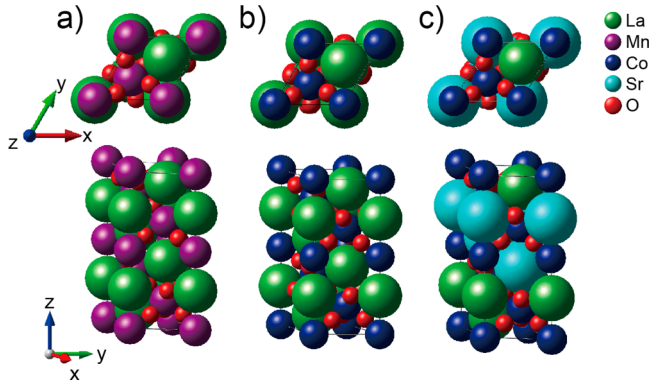

Figure 1. Crystal structure of fully relaxed (a) $LaMnO_3$ (LMO), (b) $LaCoO_3$ (LCO), and (c) $La_{0.5}Sr_{0.5}CoO_3$ (LSCO). The 1 × 1 × 1 bulk structure corresponds to the space group rhombohedral $R\bar{3}ch$, showing the atomic position of each unit cell.

To evaluate OER activity of the perovskite oxides prepared in the study, cyclic voltammetry (CV) technique with rotating disk electrode (RDE) has been used with rotation speed of 900 rpm in N_2-saturated 0.1 M KOH electrolyte measured in the potential range of 0 to 1.0 V (vs SCE), which corresponds to the region of OER ($4HO^- \rightarrow O_2 + 2H_2O + 4e^-$). Figure 3 presents the obtained OER polarization curves of the perovskite oxides with clearly different catalytic activity in terms of measured current response within the potential range. Comparing between LCO and LMO, LCO demonstrates far superior OER activity in terms of both OER potential at 1 mA cm^{-2} and OER current density at 2.0 V (vs RHE) even though both LCO and LMO possess the same $R\bar{3}ch$ rhombohedral symmetric structure. Furthermore, LSCO shows even higher OER current density by 17.4 mA cm^{-2} at 2.0 V (vs RHE) and lower overpotential for OER by 80 mV at 1 mA cm^{-2} than that of LCO (inset). These significant improvements in OER activity are attributed to partial Sr-substitution of La in the A site of the perovskite oxide. The observed trend in the OER activity of the perovskite oxides are summarized in Figure 3 in terms of OER potential at 1 mA cm^{-2} and OER current density at 2.0 V (vs RHE), which show increasing OER activity in the order of LSCO > LCO > LMO.

DOI: 10.1021/acscatal.5b00114
ACS Catal. 2015, 5, 4337−4344

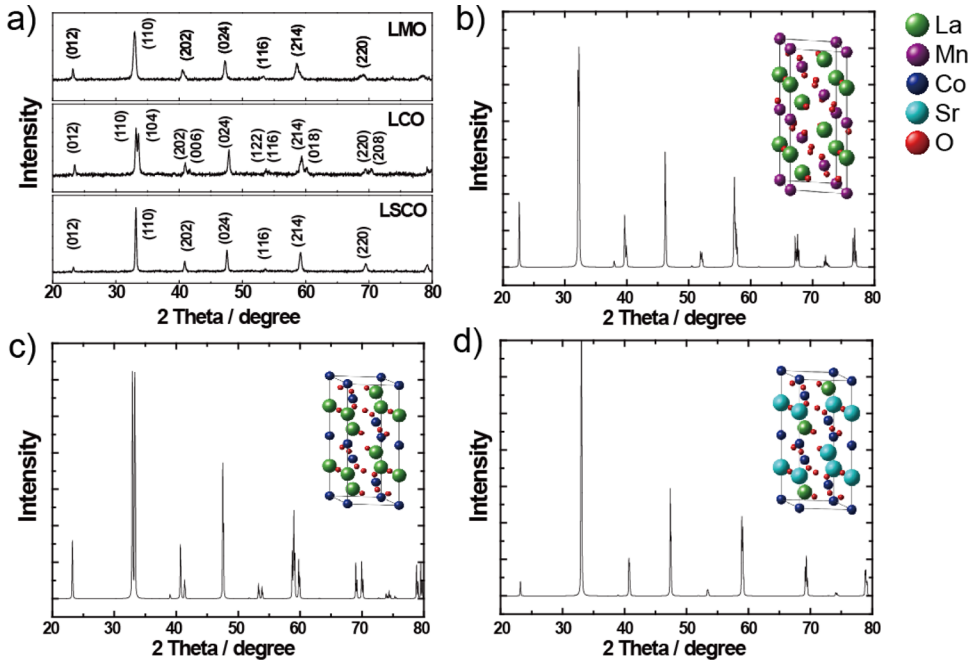

Figure 2. X-ray diffraction patterns of LMO, LCO, and LSCO: (a) experimentally measured and (b–d) calculated using lattice information obtained from the ICSD database.

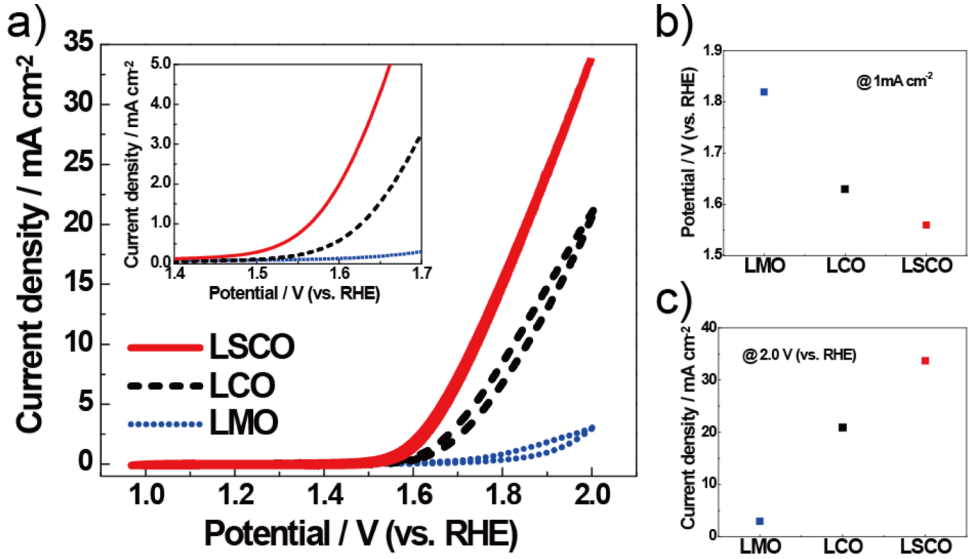

Figure 3. (a) OER polarization curves of LCO, LSCO, and LMO obtained at rotation speed of 900 rpm with 10 mV s^{-1} scan rate in N_2-saturated 0.1 M KOH solution. (inset) Potential range from 1.4 to 1.7 V. (b) OER potential measured at current density of 1 mA cm^{-2}. (c) Current density measured at 2.0 V (vs RHE) of LCO, LSCO, and LMO.

Building on the trend in the OER activity of the perovskite oxides observed from the above experimental investigation, a computational analysis by DFT has been carried out to study the exact OER mechanism. For the DFT calculations, a slab model has been designed for each perovskite oxide investigated in this study as shown in Figure S5, representing (2 × 2) unit cell of the (001) surface designed based on fully relaxed bulk structure previously illustrated in Figure 1. To determine the most stable surface of LSCO, the surface structures have been investigated by calculating the surface free energy, which can be normally approximated by method as described in Supporting Information. For instance, differently terminated surfaces of LSCO are illustrated in Figure S5 with corresponding slab model for each surface. Among them, Co terminated surface with Sr–Co–Sr underlayer as shown in Figure 4 has been selected for DFT analysis of its OER activity since it has the lowest surface energy. On this surface of each perovskite oxide, a set of adsorbed structures with oxygen intermediates (e.g., O, OH and OOH) have been fully relaxed as shown in Figure S6.

On the basis of fully relaxed structures presented above, we have studied the rate-determining step (RDS) for each oxygen intermediate reactions to reveal the origin of OER of each perovskite oxide. In alkaline condition, the proton donor may be H_2 rather than H_3O^+.[24,25] The reaction can then be expressed in terms of OH^- as follows:

$$2OH^-(aq) + H_2(g) \rightleftharpoons 2H_2O(l) + 2e^- \quad (1)$$

DOI: 10.1021/acscatal.5b00114
ACS Catal. 2015, 5, 4337–4344

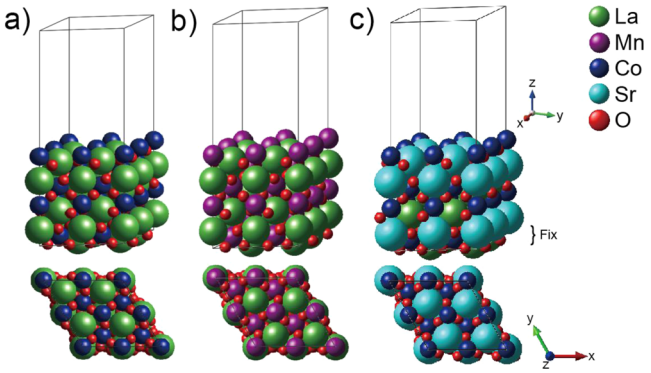

Figure 4. Schematic illustrations of (001) 13-layer slab of (a) LMO, (b) LCO, and (c) LSCO surface reaction simulations. In order to avoid energy fluctuations due to relaxation of all other terminations, we have fixed the first five layers from the bottom termination to be not involved in the surface reactions to the bulk coordinates and allowed atomic relaxation for the rest of layers.

The four electron reaction paths are then considered as shown in the following eqs 2−5:

$$4OH^- \rightleftharpoons [OH]^* + 3OH^- + e^- \quad (2)$$

$$[OH]^* + 3OH^- + e^- \rightleftharpoons O^* + H_2O(l) + 2OH^- + 2e^- \quad (3)$$

$$O^* + H_2O(l) + 2OH^- + 2e^- \rightleftharpoons OOH^* + H_2O(l) + OH^- + 3e^- \quad (4)$$

$$OOH^* + H_2O(l) + OH^- + 3e^- \rightleftharpoons O_2(g) + 2H_2O(l) + 4e^- \quad (5)$$

where * indicates that a catalyst's surface site is available for adsorption. Then the free energy of each reaction (ΔG) above has been calculated using eq 6

$$\Delta G = \Delta E + \Delta ZPE - T\Delta S \quad (6)$$

where ΔE, ΔZPE, and ΔS denote the difference in the DFT calculated ground state energy, zero point energy, and entropy corrections, respectively. The ΔZPE correction for each intermediate has been taken from the thermodynamic table reported by Nørskov et al.[26] (also, see Table S1 in the Supporting Information), using the value of ΔS corresponding to T = 298 K.[26,27] The pH effect on the potential is based on pH = 14 by shifting the electronic chemical potential according to the Nernst's law, and all potentials are expressed in terms of the reversible hydrogen electrode (RHE). From the above equations, the reversible potentials (U°) of the four reactions are calculated according to eqs 7−10 as follows:

$$\Delta G_1 = \Delta G_{OH^*} - \Delta G_{H_2O,l} + \frac{1}{2}\Delta G_{H_2} + kT \ln a_{H^+} - eU_1^\circ \quad (7)$$

$$\Delta G_2 = \Delta G_{O^*} - \Delta G_{OH^*} + \frac{1}{2}\Delta G_{H_2} + kT \ln a_{H^+} - eU_2^\circ \quad (8)$$

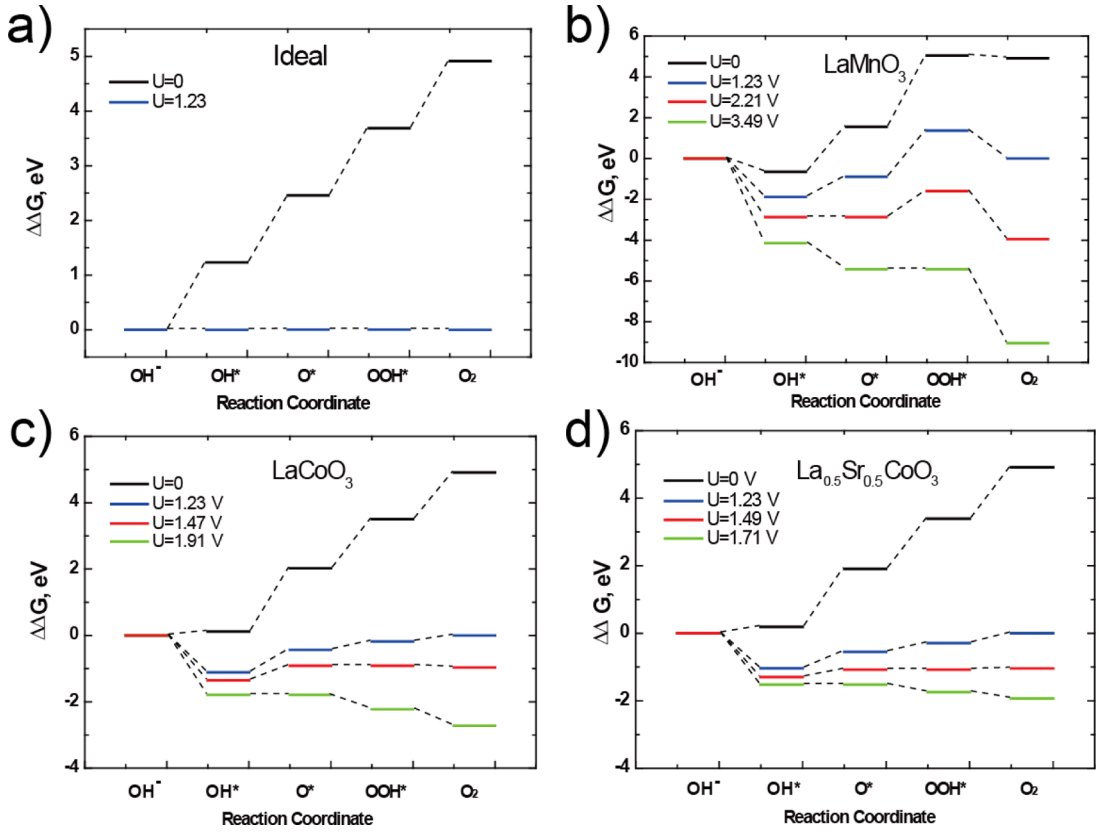

Figure 5. Standard free energy diagrams for OER obtained at zero potential (U = 0), equilibrium potential for OER (U = 1.23 V), and at the potential for which all steps proceed downward at pH 14 and T = 298 K.

DOI: 10.1021/acscatal.5b00114
ACS Catal. 2015, 5, 4337−4344

$$\Delta G_3 = \Delta G_{OOH^*} - \Delta G_{O^*} - \Delta G_{H_2O} + \frac{1}{2}\Delta G_{H_2} + kT \ln a_{H^+} - eU_3^\circ \quad (9)$$

$$\Delta G_4 = \Delta G_{O_2,g} - \Delta G_{OOH^*} + \frac{1}{2}\Delta G_{H_2} + kT \ln a_{H^+} - eU_4^\circ \quad (10)$$

where ΔG_i is the ab initio calculated free energy for oxygen intermediates denoted *i*.

On the basis of the results obtained from calculated free energy for each oxygen intermediate, Figure 5 and Table S2 shows the free energy change in each step of OER of the ideal catalyst, LMO, LCO, and LSCO at zero electrode potential (Φ = 0 V vs RHE) and reversible potential for each intermediate reaction. At the equilibrium potential (U = 1.23 V), OH* and O_2 formation is energetically downhill (exothermic), whereas all other steps are uphill (endothermic) on LMO. For LCO and LSCO, in contrast, OH* formation is energetically downhill whereas all other steps are uphill at U = 1.23 V. By applying an overpotential U > 1.23 V, the reversible potential for OH*/O* were calculated to be 2.21, 1.91, and 1.71 V vs RHE whereas those of O*/OOH* were found to be 3.49, 1.47, and 1.49 V vs RHE for LMO, LCO, and LSCO, respectively. All free energy steps of OER intermediates become relatively more negative at potentials 3.49, 1.91, and 1.71 V vs RHE for LMO, LCO, and LSCO, respectively.

Significantly lower overpotential obtained by LSCO compared to LMO and LCO is a clear indication that LSCO has superior OER activity, which is consistent with the experimental results previously shown in Figure 3. An overpotential that is even slightly lower than the potential at which every reaction step is energetically negative (i.e., U < 3.49 V vs RHE for LMO), the oxidation step from O* to OOH* becomes energetically positive (endothermic), revealing that the formation of OOH* is the rate-limiting step for OER. In contrast, the oxidation step from OH* to O* becomes uphill (endothermic) for LCO and LSCO with any overpotential lower than 1.91 and 1.71 V vs RHE, respectively, which means that the rate-limiting step is the formation of O*. These results suggest that the potential determining step as observed from the free energy diagrams is strongly dependent on the identity of the transition metal in the B site of perovskite oxide (e.g., redox behavior).

On the basis of the Sabatier principle, the interaction between the catalyst and the reactant should be neither too strong nor too weak.[28−30] Hence, the differences in the catalytic OER activity of LMO, LCO, and LSCO can explained by adsorption strength in terms of electronic structure of the materials of the oxygen intermediates on the catalyst surface. The oxygen chemisorption energy is one of main descriptors for elucidating the OER activity of the perovskite oxides. As summarized in Table S3 in the Supporting Information, the DFT adsorption energy of LMO (defined as $E^c_{ads,O}$ by eq S5) is evaluated to be −3.59 eV, which is lower than −2.37 eV of LCO and −3.24 eV of LSCO. On the basis of the potential determining step (eq 4) found in the free energy diagram of Figure 5, the lowest OER activity of LMO is likely due to relatively stronger oxygen chemisorption onto LMO surface resulting in a slow kinetics of the formation of OOH* from O. On the other hand, based on the potential determining step (eq 3) of LCO and LSCO, which represents the formation of O* from OH*, oxygen is relatively weakly adsorbed on the surface leading to higher OER activity compared to LMO. Nevertheless, the partial substitution of La atom with Sr forming LSCO lattice leads to relatively higher activity toward OER due to increased interaction between oxygen and the surface of LSCO, finely tuning the adsorption strength for oxygen.

To understand the relationship between oxygen adsorption strength and OER activity, the electronic structures of Mn and Co have been calculated to further elucidate the OER active site of the perovskite oxides.[32,33] For a wide range of materials, a simple electronic structure parameter, namely the d-band center is sufficient to understand the kinetics that govern the oxygen reduction and evolution reactions.[11,12] However, the d-band model has not been extended to explaining the catalytic activity of metal oxides because the ionic interaction between metal and nonmetal leads to more complexities in density of states (DOS). The strong chemical bonding results in split-offs of DOS into bonding and antibonding in terms of coordination number of atoms. Therefore, to understand the electronic structure of perovskite oxides, the molecular orbital theory needs to be applied for the octahedral environment which gives rise to doubly e_g and triply t_{2g} degenerated sets, which in turn consist of axial orbitals of $d_{x^2-y^2}$ and d_{z^2} and interaxial of d_{xy}, d_{xz}, and d_{yz} orbitals, respectively.[28,31] Previous literature has reported that the e_g orbital (d_{z^2}) of transition metal is mainly related to catalytic activity for ORR and OER.[28,31] Representatively, Shao-Horn and coworks proposed key factors in designing highly active perovskite oxide catalysts based on e_g (i.e., the d_{z^2} orbital) occupancy of surface-transition metal cation and its covalency with oxygen, suggesting catalytic activity-oriented elemental composition of perovskite oxides toward OER.[32,33] Similarly, Calle-Vallejo and associates have proposed that the number of outer electrons works as a good descriptor for describing trends in the adsorption energies on metal and their oxides surfaces.[22,34,35] They reported that increasing the number of outer electrons of the B site in perovskite oxides leads to weaker adsorption energies for oxygen intermediates on catalyst surface. Similar to their studies, the number of outer electrons of pure Mn and Co are 7 and 8, and those of Mn and Co in B^{3+} oxidation state are 4 and 6 in ABO_3 structure. Figure 6 shows OER current density and oxygen adsorption strength of each perovskite oxide as a function of the number of outer electrons in B^{3+}. We have simply calculated the number of valence electrons of LSCO to be 5.5 since the displacement of trivalent La^{3+} by divalent Sr^{2+} in ABO_3 leads to the formation of tetravalent Co^{4+} (See counting number of electrons in the Supporting Informa-

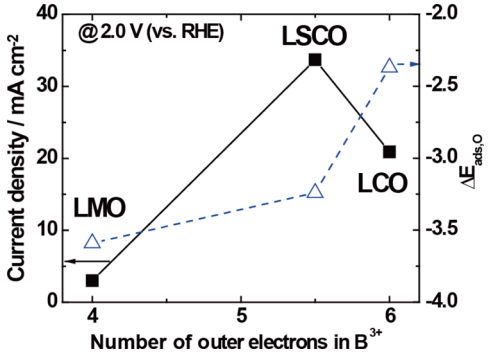

Figure 6. OER current density measured at 2.0 V (vs RHE) and the adsorption energy for O* adsorbed on LMO, LCO, and LSCO surfaces as a function of the number of outer electrons of B^{3+} in ABO_3.

DOI: 10.1021/acscatal.5b00114
ACS Catal. 2015, 5, 4337−4344

tion).[36] On the basis of Figure 6, LMO has stronger chemisorption of oxygen than LCO due to less number of outer electrons. This is verified by our DFT analysis where LMO shows the strongest chemisorption energy for oxygen among the three perovskite oxides, as well as by experimental evaluation where LMO shows the least active OER. As discussed previously, increasing the number of outer electrons should reduce the chemisorption energy for oxygen and improve OER activity; however, six outer electrons in LCO appear to be too weak as verified by intermediate OER activity. Partially substituting A site La atoms with Sr increases the oxidation state of Co (higher than Co^{3+}), which then slightly decreases the number of outer electrons from 6 to 5.5. The resulting LSCO shows the highest OER current density among the three perovskite oxides. These results confirm that the oxygen chemisorption energy can be fine-tuned by controlling the number of outer electrons of Co atoms in the B site, consistently reported in the previous literature.[8,34,35] Therefore, based on these results, highly active OER catalyst can be obtained by optimizing the oxygen chemisorption energy through chemical modification of perovskite oxide composition.

The projected-density of states (PDOS) of the 3d orbital of Mn and Co in B site has been investigated for both bulk and surface of LMO, LCO, and LSCO as shown in Figure S7. Inset in Figure S7, the total DOS of perovskite oxides reveals that spin up electrons are filled in the energy state close to the Fermi level indicative of metallic property. In contrast, no energy of density is observed near the Fermi level in spin down, showing a well-defined gap of 1.61, 1.42, and 0.45 eV for LMO, LCO, and LSCO, respectively, where lower band gap leads to improved electrical conductivity. In addition to the concept of using the number of outer electrons to elucidate the degree of electrocatalytic activity, relative positioning of the d_{z^2} orbital (e.g., e_g orbital) has been also proposed to affect catalytic performance of perovskite oxides that have octahedral environment.[28,37−40] In our previous report, we have discovered that the level of d_{z^2} orbital in a semioctahedral environment of iron phthalocyanine derived nonprecious catalyst strongly is dependent on the oxygen reduction activity.[40] On the basis of the DOS shown in Figure S7, the average position of d_{z^2} orbital of the B site atom shows a trend of upward shift with increased strength of bonding of oxygen on perovskite oxide surface, which are evaluated to be −3.70, −4.09, and −4.02 eV based on eq S7 for LMO, LCO, and LSCO, respectively. This trend shows the strongest adsorption for oxygen with LMO based on the highest average position of d_{z^2}, which shows the least favorable OER activity. On the other hand, the lowest average position of d_{z^2} obtained with LCO shows an intermediate OER activity due to relatively weak chemisorption energy for oxygen. The average position of d_{z^2} orbital of LSCO, however, is relatively upshifted than that of LCO, which enhances oxygen bonding strength, consistently observed in DFT analysis. Hence, the optimized oxygen binding energy of LSCO by introducing Sr into the A site is again confirmed by upshifting of d_{z^2} orbital level in DOS, resulting in the highest OER activity as verified by electrochemical evaluation.

In summary, using first-principles DFT calculations, we have studied scientifically relevant OER processes occurring on the surface of LMO, LCO, and LSCO perovskite oxides. The as-synthesized perovskite oxides have rhombohedrally distorted structure with $R\bar{3}ch$ space group rather than a typical cubic structure. From experimental electrochemical testing, LSCO has been revealed to demonstrate the highest OER activity in terms of both OER potential at 1 mA cm^{-2} and OER current density at 2.0 V vs RHE. On the basis of the free energy diagram, the kinetics of OER is found to be governed by the adsorption strength of oxygen intermediate species on a perovskite oxide surface where the potential determining step of LMO is the formation from O* to OOH*, and those of LCO and LSCO are the formation of O* from OH*. Among the three oxides, the calculated potential at which the free energies of formation of all oxygen intermediates are more negative (exothermal) is the lowest for LSCO, indicative of the lowest overpotential for OER. Relatively lower OER activities of LMO and LCO than LSCO, however, are due to relatively stronger and weaker adsorption strengths of oxygen on the perovskite oxide surface, respectively. Superior OER kinetics of LSCO is attributed to fine-tuned adsorption strength for oxygen, which is optimized based on the number of outer electrons of Co by partially incorporating Sr into the A site of LCO lattice, which is observed to upshift the position of d_{z^2} orbital close to the Fermi level. In order to accurately predict the activity of OER catalyst for further development, defining the exact crystal structure is essential so that the underlying electrochemical reaction mechanism can be understood through experimental studies and theoretical design. On the basis of this synergetic approach of combining experimental and computational investigations, highly active OER catalysts can be obtained by appropriately selecting B site atom and further modifying A site atom of perovskite oxides to fine-tune the oxygen chemisorption energy based on the number of valence electrons and the level of e_g orbital.

METHOD

Computational Details. Density functional theory (DFT)[41,42] calculations implemented in Vienna ab initio simulation package (VASP)[43] program were utilized for the present study. Exchange-correlation energies of electrons were described by the Perdew, Burke, and Ernzerhof (PBE) functional[44] for generalized gradient approximation (GGA).[45] Core electrons were replaced by the projector augmented wave (PAW) pseudopotentials,[46,47] and Kohn−Sham wave functions of valence electrons were expanded by plane wave basis set with a cutoff energy of 520 eV. This density functional level of theory had previously well predicted trends in formation energy of rutile[48] and perovskite oxide[22] structures. In addition, the Hubbard U parameter (GGA+U) was employed to improve the description of correlation effects and to reduce the self-interaction error.[17,49,50] The optimized effective interaction parameter U_{eff} ($U_{eff} = U - J$) of 3.9 and 3.4 eV were used for Mn and Co transition metals in $LaXO_3$ (X: Mn and Co) structure. These values have previously been shown to provide a description of $LaXO_3$ electronic structure that is in good agreement with the available experimental data.[17] The atoms and cell parameters of each structure were fully relaxed, and spin polarized calculations were performed. All ions were fully relaxed during the structural optimization until the total energy was converged within 10^{-4} eV. A gamma point mesh with (15 × 15 × 15) k-points was used for the $LaMnO_3$, $LaCoO_3$, and $La_{0.5}Sr_{0.5}CoO_3$ (1 × 1) unit cell to sample the Brillouin zone for bulk calculation. Periodic boundary conditions were imposed on these unit cells in terms of (001) surface direction, and a vacuum space of 20 Å was employed to avoid interactions between top and bottom surface. The first five layers have been fixed from the bottom and the rest of layers were relaxed. For calculate the total energies of $LaMnO_3$, $LaCoO_3$, and

DOI: 10.1021/acscatal.5b00114
ACS Catal. 2015, 5, 4337−4344

$La_{0.5}Sr_{0.5}CoO_3$ slab models on (001) surface direction, gamma point mesh of (5 × 5 × 1), and the Methfessel-Paxton smearing method were utilized.[51] For the density of states (DOS) calculations, the tetrahedron method with Blçchl's corrections[52] was employed.

Preparation of Perovskite Oxides and Its Physicochemical Analysis. One-pot synthesis of perovskite oxide nanoparticle was utilized by a solution-based simple calcination method as described in Figure S2. Metal nitrates of appropriate mole ratio corresponding to the desired perovskite oxide composition were completely dissolved in H_2O and C_2H_5OH with 1:1 mass ratio along with 16.7 wt % PVP. For example, in order to synthesize $La_{0.5}Sr_{0.5}CoO_3$, 0.5 mmol of $La(NO_3)_3 \cdot 6H_2O$, 0.5 mmol of $Sr(NO_3)_2$, and 1.0 mmol of $Co(NO_3)_2 \cdot 6H_2O$ were dissolved in the solvent. For preparation of $LaMnO_3$ and $LaCoO_3$, 1.0 mmol of $La(NO_3)_3 \cdot 6H_2O$, and 1.0 mmol of $Co(NO_3)_2 \cdot 6H_2O$ or $Mn(NO_3)_2 \cdot 4H_2O$ were dissolved in the same solvent. These solutions were placed into a quartz tube which was then laid in the center of a horizontal tube furnace. The calcination at 973 K for LMO and LCO, and at 1173 K for LSCO was carried out with ramping rate of 1 °C min^{-1} for 3 h. The furnace was cooled down to room temperature, followed by collecting of perovskite oxide powder. Before characterizing the synthesized perovskite oxide physicochemically and electrochemically, the perovskite oxides were ground by hands in a mortar. For physicochemical characterizations of perovskite oxides, the following tools were utilized in this study. X-ray diffraction (XRD, AXS D8 Advance, Brunker) and X-ray photoelectron spectroscopy (XPS, Thermal Scientific K-Alpha XPS spectrometer) were conducted for the characterization of crystalline phase and atomic compositional analysis, respectively.

Electrochemical Analysis in Detail. The electrocatalytic activity was evaluated by rotating disk electrode (RDE) measurement by a potentiostat (CH Instrument 760D) and a rotation speed controller (Pine Instrument Co., AFMSRCE). The catalyst inks were prepared with 4 mg mL^{-1} of concentration of the perovskite oxide catalyst and Vulcan carbon (VC) mixture (1:1 mass ratio) in ethanol-diluted 0.1 wt % Nafion solution and coated on a glassy carbon disk electrode (5 mm OD) with 20 μL of the ink (loading 0.41 mg cm^{-2}) to be used as working electrode. VC was employed in order to improve electrical conductivity and dispersion of perovskite oxides.[53,54] Saturated calomel electrode (SCE) and platinum (Pt) wire were utilized as reference and counter electrodes, respectively, and 0.1 M KOH was used as the electrolyte. Cyclic voltammetry (CV) was used to examine OER activities with 900 rpm in RDE measurement in N_2-saturated 0.1 M KOH at a scan rate of 5 mV s^{-1}. Although SCE was used as reference electrode, all potentials were displayed in this work vs reversible hydrogen electrode (RHE) to express pH independent electrochemical potential. The conversion equation used was $E_{RHE} = E_{SCE} + 0.241\ V + 0.059pH$, with the pH of 0.1 M KOH being 13.

■ ASSOCIATED CONTENT

Supporting Information

The Supporting Information is available free of charge on the ACS Publications website at DOI: 10.1021/acscatal.5b00114.

Surface energy calculation details, investigation of oxygen adsorption energy on perovskite oxide surfaces, counting the number of outer electrons of B site atom, calculation of the average of d_{z^2} orbital, Tables S1−S3, and Figures S1−S7 (PDF)

■ AUTHOR INFORMATION

Corresponding Author

*E-mail address: zhwchen@uwaterloo.ca. Tel.: +1-519-888-4567 ext. 38664. Fax: +1-519-746-4347.

Author Contributions

†M.H.S. and H.W.P. contributed equally to this work

Notes

The authors declare no competing financial interest.

■ ACKNOWLEDGMENTS

This work was financially supported by the Natural Sciences and Engineering Research Council of Canada (NSERC), the Canada Research Chairs Program, and the University of Waterloo. This research was also enabled by the use of computing resources provided by WestGrid and Compute/Calcul Canada and Korea Institute of Science and Technology Information (KISTI, KSC-2013-C2-054).

■ REFERENCES

(1) Zheng, J.; Tian, J.; Wu, D.; Gu, M.; Xu, W.; Wang, C.; Gao, F.; Engelhard, M. H.; Zhang, J.-G.; Liu, J.; Xiao, J. *Nano Lett.* **2014**, *14*, 2345−2352.

(2) Zhou, X. J.; Qiao, J. L.; Yang, L.; Zhang, J. J. *Adv. Energy Mater.* **2014**, DOI: 10.1002/aenm.201301523.

(3) Lee, J. S.; Kim, S. T.; Cao, R.; Choi, N. S.; Liu, M.; Lee, K. T.; Cho, J. *Adv. Energy Mater.* **2011**, *1*, 34−50.

(4) Wang, H.; Maiyalagan, T.; Wang, X. *ACS Catal.* **2012**, *2*, 781−794.

(5) Higgins, D. C.; Hoque, M. A.; Hassan, F.; Choi, J. Y.; Kim, B.; Chen, Z. W. *ACS Catal.* **2014**, *4*, 2734−2740.

(6) Hamdani, M.; Singh, R. N.; Chartier, P. *Int. J. Electrochem. Sci.* **2010**, *5*, 556−577.

(7) Li, Y. G.; Gong, M.; Liang, Y. Y.; Feng, J.; Kim, J. E.; Wang, H. L.; Hong, G. S.; Zhang, B.; Dai, H. J. *Nat. Commun.* **2013**, *4*, 1805.

(8) Suntivich, J.; May, K. J.; Gasteiger, H. A.; Goodenough, J. B.; Shao-Horn, Y. *Science* **2011**, *334*, 1383−1385.

(9) Lee, Y.; Suntivich, J.; May, K. J.; Perry, E. E.; Shao-Horn, Y. *J. Phys. Chem. Lett.* **2012**, *3*, 399−404.

(10) Chen, Z.; Higgins, D.; Yu, A.; Zhang, L.; Zhang, J. *Energy Environ. Sci.* **2011**, *4*, 3167.

(11) Greeley, J.; Stephens, I. E. L.; Bondarenko, A. S.; Johansson, T. P.; Hansen, H. A.; Jaramillo, T. F.; Rossmeisl, J.; Chorkendorff, I.; Nørskov, J. K. *Nat. Chem.* **2009**, *1*, 552−556.

(12) Hammer, B.; Nørskov, J. K. Theoretical surface science and catalysis−calculations and concepts. *Advances in Catalysis*; Elsevier, 2000; Vol. *45*, pp 71−129.

(13) Seo, M. H.; Choi, S. M.; Lim, E. J.; Kwon, I. H.; Seo, J. K.; Noh, S. H.; Kim, W. B.; Han, B. *ChemSusChem* **2014**, *7*, 2609−2620.

(14) Higgins, D.; Hoque, M. A.; Seo, M. H.; Wang, R.; Hassan, F.; Choi, J.-Y.; Pritzker, M.; Yu, A.; Zhang, J.; Chen, Z. *Adv. Funct. Mater.* **2014**, *24*, 4325−4336.

(15) Seo, J. K.; Khetan, A.; Seo, M. H.; Kim, H.; Han, B. *J. Power Sources* **2013**, *238*, 137−143.

(16) Sanchez, J. M.; Ducastelle, F.; Gratias, D. *Phys. A* **1984**, *128 A*, 334−350.

(17) Hautier, G.; Ong, S. P.; Jain, A.; Moore, C. J.; Ceder, G. *Phys. Rev. B: Condens. Matter Mater. Phys.* **2012**, *85*, 155208.

(18) Tan, T. L.; Wang, L.-L.; Johnson, D. D.; Bai, K. *Nano Lett.* **2012**, *12*, 4875−4880.

(19) Han, B.; Viswanathan, V.; Pitsch, H. *J. Phys. Chem. C* **2012**, *116*, 6174−6183.

(20) Zhou, F.; Cococcioni, M.; Marianetti, C. A.; Morgan, D.; Ceder, G. *Phys. Rev. B: Condens. Matter Mater. Phys.* **2004**, *70*, 235121.

DOI: 10.1021/acscatal.5b00114
ACS Catal. 2015, 5, 4337−4344

(21) Wang, Y.; Cheng, H. P. *J. Phys. Chem. C* **2013**, *117*, 2106−2112.
(22) Calle-Vallejo, F.; Martinez, J. I.; Garcia-Lastra, J. M.; Mogensen, M.; Rossmeisl, J. *Angew. Chem., Int. Ed.* **2010**, *49*, 7699−7701.
(23) Sunarso, J.; Torriero, A. A. J.; Zhou, W.; Howlett, P. C.; Forsyth, M. *J. Phys. Chem. C* **2012**, *116*, 26108−26108.
(24) Rossmeisl, J.; Logadottir, A.; Nørskov, J. K. *Chem. Phys.* **2005**, *319*, 178−184.
(25) Hansen, H. A.; Rossmeisl, J.; Nørskov, J. K. *Phys. Chem. Chem. Phys.* **2008**, *10*, 3722−3730.
(26) Nørskov, J. K.; Rossmeisl, J.; Logadottir, A.; Lindqvist, L.; Kitchin, J. R.; Bligaard, T.; Jónsson, H. *J. Phys. Chem. B* **2004**, *108*, 17886−17892.
(27) Atkins, P.; Paula, J. D. *Physical Chemistry*, eighht ed.; Oxford University Press: Oxford, UK, 2006.
(28) Ramaswamy, N.; Tylus, U.; Jia, Q.; Mukerjee, S. *J. Am. Chem. Soc.* **2013**, *135*, 15443−15449.
(29) Bing, Y.; Liu, H.; Zhang, L.; Ghosh, D.; Zhang, J. *Chem. Soc. Rev.* **2010**, *39*, 2184−2202.
(30) Mani, P.; Srivastava, R.; Strasser, P. *J. Power Sources* **2011**, *196*, 666−673.
(31) Huheey, J. E.; Keiter, E. A.; Keiter, R. L. *Inorganic Chemistry: Principles of Structure and Reactivity*; Prentice Hall: London, 1997.
(32) Man, I. C.; Su, H. Y.; Calle-Vallejo, F.; Hansen, H. A.; Martinez, J. I.; Inoglu, N. G.; Kitchin, J.; Jaramillo, T. F.; Norskov, J. K.; Rossmeisl, J. *ChemCatChem* **2011**, *3*, 1159−1165.
(33) Suntivich, J.; Gasteiger, H. A.; Yabuuchi, N.; Nakanishi, H.; Goodenough, J. B.; Shao-Horn, Y. *Nat. Chem.* **2011**, *3*, 546−550.
(34) Calle-Vallejo, F.; Díaz-Morales, O. A.; Kolb, M. J.; Koper, M. T. M. *ACS Catal.* **2015**, *5*, 869−873.
(35) Calle-Vallejo, F.; Inoglu, N. G.; Su, H. Y.; Martınez, J. I.; Man, I. C.; Koper, M. T. M.; Kitchin, J. R.; Rossmeisl, J. *Chem. Sci.* **2013**, *4*, 1245.
(36) Jonker, G. H.; Santen, J. H. V. *Physica* **1953**, *19*, 120−130.
(37) Zagal, J.; Bindra, P.; Yeager, E. *J. Electrochem. Soc.* **1980**, *127*, 1506−1517.
(38) Zagal, J.; Paez, M.; Tanaka, A. A.; Dossantos, J. R.; Linkous, C. A. *J. Electroanal. Chem.* **1992**, *339*, 13−30.
(39) Ramaswamy, N.; Mukerjee, S. *Adv. Phys. Chem.* **2012**, *2012*, 1.
(40) Seo, M. H.; Higgins, D.; Jiang, G.; Choi, S. M.; Han, B.; Chen, Z. *J. Mater. Chem. A* **2014**, *2*, 19707−19716.
(41) Hohenberg, P.; Kohn, W. *Phys. Rev.* **1964**, *136*, B864−B871.
(42) Kohn, W.; Sham, L. J. *Phys. Rev.* **1965**, *140*, A1133−A1138.
(43) Kresse, G.; Furthmüller, J. *Phys. Rev. B: Condens. Matter Mater. Phys.* **1996**, *54*, 11169.
(44) Perdew, J. P.; Burke, K.; Ernzerhof, M. *Phys. Rev. Lett.* **1996**, *77*, 3865.
(45) Kresse, G.; Furthmuller, J. *Comput. Mater. Sci.* **1996**, *6*, 15−50.
(46) Kresse, G.; Joubert, D. *Phys. Rev. B: Condens. Matter Mater. Phys.* **1999**, *59*, 1758.
(47) Blöchl, P. E. *Phys. Rev. B: Condens. Matter Mater. Phys.* **1994**, *50*, 17953.
(48) Martinez, J. I.; Hansen, H. A.; Rossmeisl, J.; Norskov, J. K. *Phys. Rev. B: Condens. Matter Mater. Phys.* **2009**, DOI: 10.1103/PhysRevB.79.045120.
(49) Franchini, C.; Podloucky, R.; Paier, J.; Marsman, M.; Kresse, G. *Phys. Rev. B: Condens. Matter Mater. Phys.* **2007**, DOI: 10.1103/PhysRevB.75.195128.
(50) Lee, Y. L.; Kleis, J.; Rossmeisl, J.; Morgan, D. *Phys. Rev. B: Condens. Matter Mater. Phys.* **2009**, DOI: 10.1103/PhysRevB.80.224101.
(51) Methfessel, M.; Paxton, A. T. *Phys. Rev. B: Condens. Matter Mater. Phys.* **1989**, *40*, 3616−3621.
(52) Blöchl, P. E.; Jepsen, O.; Andersen, O. K. *Phys. Rev. B: Condens. Matter Mater. Phys.* **1994**, *49*, 16223−16233.
(53) Park, H. W.; Lee, D. U.; Zamani, P.; Seo, M. H.; Nazar, L. F.; Chen, Z. *Nano Energy* **2014**, *10*, 192−200.
(54) Park, H. W.; Lee, D. U.; Park, M. G.; Ahmed, R.; Seo, M. H.; Nazar, L. F.; Chen, Z. *ChemSusChem* **2015**, *8*, 1058−1065.

DOI: 10.1021/acscatal.5b00114
ACS Catal. 2015, 5, 4337−4344